Physica D 280–281 (2014) 73–85

Contents lists available at ScienceDirect

Physica D

journal homepage: www.elsevier.com/locate/physd

Dynamics of the wave turbulence spectrum in vibrating plates: A numerical investigation using a conservative finite difference scheme

Michele Ducceschi [a], Olivier Cadot [a], Cyril Touzé [a,*], Stefan Bilbao [b]

[a] Unité de Mécanique (UME), Ensta-ParisTech, 828, Boulevard des Maréchaux, 91762 Palaiseau Cedex, France
[b] Room 7306B, James Clerk Maxwell Building, King's Buildings, Mayfield Rd., Edinburgh EH9 3JZ, UK

HIGHLIGHTS

- Non-stationary wave turbulence in a vibrating plate is numerically studied.
- Self-similar dynamics of the spectra are found with and without periodic external forcing.
- The self-similar solutions are in agreement with the kinetic equation.
- A realistic geometric imperfection is shown to have no effect on the global properties.

ARTICLE INFO

Article history:
Received 19 November 2013
Received in revised form
12 April 2014
Accepted 25 April 2014
Available online 10 May 2014
Communicated by M. Vergassola

Keywords:
Non-stationary wave turbulence
Elastic plate
Imperfections
Pointwise forcing
Finite difference
Conservative scheme

ABSTRACT

The dynamics of the local kinetic energy spectrum of an elastic plate vibrating in a wave turbulence (WT) regime is investigated with a finite difference, energy-conserving scheme. The numerical method allows the simulation of pointwise forcing together with realistic boundary conditions, a set-up which is close to experimental conditions. In the absence of damping, the framework of non-stationary wave turbulence is used. Numerical simulations show the presence of a front propagating to high frequencies, leaving a steady spectrum in its wake. Self-similar dynamics of the spectra are found with and without periodic external forcing. For the periodic forcing, the mean injected power is found to be constant, and the frequency at the cascade front evolves linearly with time resulting in a increase of the total energy. For the free turbulence, the energy contained in the cascade remains constant while the frequency front increases as $t^{1/3}$. These self-similar solutions are found to be in accordance with the kinetic equation derived from the von Kármán plate equations. The effect of the pointwise forcing is observable and introduces a steeper slope at low frequencies, as compared to the unforced case. The presence of a realistic geometric imperfection of the plate is found to have no effect on the global properties of the spectra dynamics. The steeper slope brought by the external forcing is shown to be still observable in a more realistic case where damping is added.

1. Introduction

Wave Turbulence (WT) describes a system of waves interacting nonlinearly away from thermodynamical equilibrium [1,2]. Although the system under study is composed of waves only, the term "turbulence" is used here in analogy with hydrodynamic turbulence, where the energy of the system is transferred through scales (referred to as a cascade) resulting in a large bandwidth energy spectrum. A particular property is that, for WT systems, the form of the spectrum can be derived analytically [3] and not just in terms of dimensional analysis as for the Kolmogorov 41 theory of hydrodynamics turbulence [4]. Using the assumption of weak nonlinearity, and an appropriate separation of timescales, a natural closure arises leading to an analytical expression for the equation for the second order moment (*e.g.* the kinetic energy spectrum). Solutions to this equation lead to two physically different scenarios: the first one represents the system at equilibrium, where the total energy of the system is equally spread among all the Fourier components of the system (known as the modes), and thus corresponding to a Rayleigh–Jeans type of spectrum. The second scenario is out-of-equilibrium and leads to the Kolmogorov–Zakharov spectrum that describes a flux of energy from the injection scale, where energy is input in the system, to the dissipation scale such as in hydrodynamics turbulence. In the latter scenario the modes re-

* Corresponding author. Tel.: +33 1 69 31 97 34; fax: +33 1 69 31 99 97.
E-mail address: cyril.touze@ensta-paristech.fr (C. Touzé).

http://dx.doi.org/10.1016/j.physd.2014.04.008
0167-2789/

ceive and give energy to adjacent modes, thus creating a cascade of energy through scales. WT formalism has been applied to many systems in a variety of contexts, ranging from quantum-mechanical to astrophysical systems, and includes many systems encountered in the ordinary world. An exhaustive list may be found in [1]; here some examples are recalled: capillary [5,6] and surface gravity waves [7–9], Alfvén waves [10,11], and Kelvin waves [12,13].

Flexural waves produced by large amplitude vibrations of elastic plates have been studied within the framework of the wave turbulence theory [14] applied to the von Kármán equation [15,16] for the transverse displacement w. The analytical Kolmogorov–Zakharov spectrum is then given by

$$P_v(f) = \frac{Ch}{(1-\nu^2)^{2/3}} \varepsilon_c^{1/3} \log^{1/3}\left(\frac{f_c^\star}{f}\right); \tag{1}$$

where ε_c is the constant flux of energy transferred through scales, P_v refers to the power spectrum of the transverse velocity $v = \dot{w}$, h is the thickness of the plate, ν Poisson's ratio of the material, and C a constant. Because the theory is fully inertial, $f_c^\star$ is the frequency at which energy is removed from the system. In experiments, this is ensured by the damping of the plate. At first order the spectrum is flat, but with a log-correction in the inertial range of frequencies. The WT theoretical result has been compared to experiments [17,18], showing discrepancies regarding the shape and scaling of the spectrum with the energy flux. Thus, recent work has focused on the investigation of the possible causes for such discrepancies. Experimentally, the wave-structure and dispersion relation was checked in [18], leading to the conclusion that the nonlinear vibrations of a plate are indeed due to a set of waves following the theoretical (linear) dispersion relation. The correct separation of timescales, necessary assumption for the WT theory, was verified in [19]. A first discrepancy effect was observed in [20], showing that the local forcing of the shaker is responsible for a steeper slope in the supposed inertial range of the energy spectra. More recently, damping has also been shown to be the cause for a steeper slope of the spectrum, indicating that the inertial range might not exist for thin plates used in experiments, rendering then meaningless any comparison with the WT theory [21]. From the numerical standpoint, it is worth mentioning that all the numerical methods used so far are spectral schemes [14,22,21,23–25]. Hence the forcing is in the Fourier space, a feature that is different from a pointwise excitation used in experimental conditions. All available numerical results recover the KZ spectrum of Eq. (1) when the damping is localized at high frequency only. However, when realistic damping is added, see *e.g.* [21,23], the same conclusions as for the experiment are met.

Other sources of discrepancies have not been addressed yet, such as the finite size effects or the possibility of three wave interactions (quadratic nonlinearities) in real plates. Because of the $w \to -w$ symmetry of the von Kármán equation, these nonlinearities are not taken into account in [14]. Indeed, geometrical imperfections are unavoidable in real plates, and they are known to break this symmetry and to produce quadratic nonlinearities [26,27]. In particular, it has been shown in [28,29] that imperfections play an important role in the transition scenario to turbulence and favor instabilities and the appearance of quasiperiodic vibrations.

The numerical method used in this work relies on a finite difference, time domain, energy-conserving scheme [30,29]. The main advantages are that: (i) the time-stepping integration method conserves energy up to machine accuracy, so that essential properties of the underlying continuous Hamiltonian systems are preserved by the discretization [31]; (ii) the external forcing is pointwise in space just as in the real experiments; (iii) realistic boundary conditions can be implemented instead of using periodic boundary conditions as considered by previous numerical investigations using spectral methods [14,22,25].

The aim of this article is to investigate numerically wave turbulence produced by the von Kármán plate equations. With a numerical scheme close to experimental conditions, unavoidable effects in real experiments such as pointwise forcing and geometric imperfections can be accounted for. In order to properly distinguish the different effects, most of the presented results are obtained in the absence of damping, where the framework of non-stationary wave turbulence should be used [32,33]. The theory predicts self-similar dynamics of the spectra with a front propagating to higher frequencies. Such propagation has been observed for surface gravity waves in experiments [34]. On the contrary, capillary turbulence [35,36] exhibits a decay that begins from the high frequency end of the spectral range. The discrepancy with the self-similar theory of wave turbulence is ascribed to the presence of finite damping at all frequencies of the wave system [35,37].

The article is organized as follows: the governing equations together with the numerical approach are described in Section 2. Section 3 presents the data analysis tools used to study the spectral dynamics. The main results are given in Section 4. Periodically forced turbulence for a perfect plate is first considered. A self-similar propagation of a steep front towards the high frequencies, leaving in its wake a steady spectrum, is observed. The frequency of the front is found to evolve linearly with time. The presence of realistic geometric imperfections is then taken into account and shown to have no influence on the spectral dynamics. In Section 4.2, the case of a free, undamped turbulence is exhibited. In that case, self-similar dynamics of the spectra are also observed, but now the front evolves with time as $t^{1/3}$. Self-similar solutions derived from the kinetic equation are found to display the same dependences, thus validating the numerical results that give in addition the shape of the self-similar function. The pointwise forcing is found to influence the shape of the universal spectrum left in the wake of the front, with a steeper slope for the forced case. Finally, the effect of the pointwise forcing, underlined in the undamped cases, is confirmed in Section 4.3, where a decaying turbulence with a simple frequency-independent damping law is addressed. Discussion and concluding remarks appear in Section 5.

2. Dynamical equations

2.1. Continuous time and space equations

The system under study is a rectangular elastic plate of thickness h, dimensions L_x, L_y, volume density ρ, Poisson's ratio ν and Young's modulus E. Its flexural rigidity is defined as $D = \frac{Eh^3}{12(1-\nu^2)}$. The dynamics of weakly nonlinear waves for the transverse displacement $w(\mathbf{x}, t)$ can be described by the von Kármán equations [15,16]. The general case of an imperfect plate is here considered. If $w_0(\mathbf{x})$ denotes the initial (static) imperfection, then the equations of motion read [26,38,27]

$$D\Delta\Delta w + \rho h \ddot{w} = L(w + w_0, F) + \mathcal{F}(\mathbf{x}, t) - R(\dot{w}, t), \tag{2a}$$

$$\Delta\Delta F = -\frac{Eh}{2} L(w + 2w_0, w), \tag{2b}$$

where Δ is the Laplacian operator, $\Delta a(\mathbf{x}) = a_{,xx} + a_{,yy}$, and $L(\cdot,\cdot)$ is the bilinear symmetric von Kármán operator, $L(a(\mathbf{x}), b(\mathbf{x})) = a_{,xx}\, b_{,yy} + a_{,yy}\, b_{,xx} - 2a_{,xy}\, b_{,xy}$. $F(\mathbf{x}, t)$ is an auxiliary function called the Airy stress function which encapsulates the behavior of the plate in the in-plane direction, $R(\mathbf{x}, t)$ is a loss factor of some kind which will be specified shortly and $\mathcal{F}(\mathbf{x}, t)$ is the external excitation load. In this work, the material parameters are chosen to correspond to a steel plate; thus $E = 2 \times 10^{11}$ Pa, $\rho = 7860$ kg/m^3, $\nu = 0.3$. The other geometrical and physical parameters will be reported case by case.

The dynamics of the plate is not complete until the boundary conditions are not selected. Physical boundary conditions can be derived by conducting an energy analysis based on the Lagrangian of the system [16,39,40]. For this work, the particular case of a transversely simply supported plate with movable in-plane edges is considered. In turn, the following conditions hold along the boundary ∂S

$$w = w_{,nn} = 0 \quad \forall \mathbf{x} \in \partial S, \tag{3a}$$

$$F = F_{,n} = 0 \quad \forall \mathbf{x} \in \partial S, \tag{3b}$$

where n is the direction normal to the boundary. This is an important difference with respect to previously presented numerical simulations, where periodic boundary conditions were employed.

The term $R(\mathbf{x}, t)$ represents losses. An artificial damping law may be used,

$$R(\dot{w}, t) = 2\sigma_0 \dot{w}, \tag{4}$$

that dissipates energy at equal rates at all scales. In the context of time-domain simulations of damped plates, the problem of an accurate representation of the damping law with an ad-hoc time operator is complex and has led numerous authors to various laws, the implementation of which still remains a numerical challenge; see *e.g.* [41]. Here the simplest time-domain operator has been chosen allowing us to explore numerically its effect on the dynamics of the cascade. The reader should however keep in mind that it is ad-hoc and does not correspond to a real case.

The forcing is pointwise and of the form:

$$\mathcal{F}(\mathbf{x}, t) = \delta(\mathbf{x} - \mathbf{x}_{\mathcal{F}}) A(t) \sin(2\pi f_p t). \tag{5}$$

The injection point has been chosen at $\mathbf{x}_{\mathcal{F}} = (0.42L_x, 0.57L_y)$ for all the simulations. The forcing frequency f_p is selected to be close to the fourth eigenfrequency of the system, in order to activate the cascade more easily [29]. $A(t)$ is chosen to be:

$$A(t) = \begin{cases} A_0\, t/t_0 & \text{for } 0 \le t \le t_0; \\ A_0 & \text{for } t_0 \le t \le t_1; \\ 0 & \text{for } t \ge t_1. \end{cases} \tag{6}$$

In the above definition, t_0 corresponds to the ramp time: the forcing ramps linearly from zero up to A_0 in t_0 seconds. Then, the forcing remains constant at A_0 for $t_1 - t_0$ seconds, where t_1 corresponds to the total length of the simulation in the case of periodic forcing.

The injected power is defined in this work as

$$\varepsilon(t) = \mathcal{F}(\mathbf{x}, t) \cdot \dot{w}(\mathbf{x}_p, t)/\rho S. \tag{7}$$

After division by the factor ρS, where $S = L_x L_y$ is the area of the plate, the injected power has the dimension of a velocity cubed.

2.2. Finite difference time domain scheme

In this section the numerical solution to system (2) together with boundary conditions (3) is presented. Although numerical simulations of von Kármán plates in the context of WT have been successfully developed in previous studies [14,22,25,23,24], here a time domain simulation in physical space is presented. Time and space are discretized so that the continuous variables (x, y, t) are approximated by their discrete counterparts $(l\delta x, m\delta y, n\delta t)$, where (l, m, n) are integer indices and $(\delta x, \delta y, \delta t)$ are the steps. Boundedness of the domain implies that $(l, m) \in [0, N_x] \times [0, N_y]$ so that the grid size is given by $(N_x + 1) \times (N_y + 1)$. The continuous variables $w(\mathbf{x}, t), F(\mathbf{x}, t)$ are then approximated by $w^n_{l,m}, F^n_{l,m}$ at the discrete time n for the grid point (l, m). Time shifting operators are introduced as

$$e_{t+} w^n_{l,m} = w^{n+1}_{l,m}, \qquad e_{t-} w^n_{l,m} = w^{n-1}_{l,m}. \tag{8}$$

Time derivatives can then be approximated by

$$\delta_{t\cdot} = \frac{1}{2h_t}(e_{t+} - e_{t-}), \qquad \delta_{t+} = \frac{1}{h_t}(e_{t+} - 1),$$

$$\delta_{t-} = \frac{1}{h_t}(1 - e_{t+}), \qquad \delta_{tt} = \delta_{t+}\delta_{t-}. \tag{9}$$

Time averaging operators are introduced as

$$\mu_{t+} = \frac{1}{2}(e_{t+} + 1), \qquad \mu_{t-} = \frac{1}{2}(1 + e_{t-}),$$

$$\mu_{t\cdot} = \frac{1}{2}(e_{t+} + e_{t-}), \qquad \mu_{tt} = \mu_{t+}\mu_{t-}. \tag{10}$$

Similar definitions hold for the space operators. Hence, the Laplacian Δ and the double Laplacian $\Delta\Delta$ are given by

$$\delta_\Delta = \delta_{xx} + \delta_{yy}, \qquad \delta_{\Delta\Delta} = \delta_\Delta \delta_\Delta. \tag{11}$$

The von Kármán operator at interior points $L(w, F)$ can then be discretized as

$$l(w, F) = \delta_{xx} w \delta_{yy} F + \delta_{yy} w \delta_{xx} F - 2\mu_{x-}\mu_{y-}(\delta_{x+y+} w \delta_{x+y+} F). \tag{12}$$

Thus the discrete counterpart of (2) is

$$D\delta_{\Delta\Delta} w + \rho h \delta_{tt} w = l(w + w_0, \mu_{t\cdot} F) + P^n_{l,m} - R^n_{l,m}; \tag{13a}$$

$$\mu_{t-} D \delta_{\Delta\Delta} F = -\frac{Eh}{2} l(e_{t-}(w + 2w_0), w). \tag{13b}$$

The damping terms are

$$r_0(l, m, n) = 2\sigma_0 \delta_{t\cdot} w^n_{l,m}; \qquad r_1(l, m, n) = -2\sigma_1 \delta_\Delta w^n_{l,m}. \tag{14}$$

When $\sigma_0 = 0$, the scheme is energy conserving, where the discrete energy is positive definite and yields a stability condition, as proved in [30,42]. Implementation of boundary conditions is explained thoroughly in [42].

3. Data analysis

The work is focused on the turbulent response at one point of the plate chosen as $(0.3L_x, 0.2L_y)$. The kinetic energy spectrum is given by the velocity power spectrum which is calculated starting from a velocity discrete-time series. For the remainder of the paper, the symbol v_n will identify the discrete velocity at the output point, at the time $t = n\delta t$. Spectra analyses are performed on time windows of duration τ. The discrete-time velocity power spectrum is then defined as:

$$P_v(f) = \frac{(\delta t)^2}{\tau} \left| \sum_{n=1}^{N} v_n e^{-i2\pi f n} \right|^2 \tag{15}$$

where $N = \tau/\delta t$ is the total number of samples within the time window. For the typical case of a thickness $h = 1$ mm and surface 0.4×0.6 m^2, the sampling frequency is chosen as $1/\delta t = 400$ kHz and a time window of $\tau = 0.05$ s is selected for the analysis of the spectra. In order to obtain a better convergence of the shape of the spectra, a mean is taken over $M = 3$ consecutive spectra; in other words, the symbol $\langle P_v(f) \rangle$ will identify the mean take over 3 spectra covering a total time window $T = M\tau$. When the thickness of the plate changes, time window and sampling frequency change accordingly. So, for instance, for a thickness $h = 0.1$ mm, the time window is multiplied by a factor of 10, $\tau = 0.5$ s and the sampling frequency is divided by a factor of 10, $1/\delta t = 40$ kHz. The number M remains instead fixed. In the following, the brackets $\langle \cdots \rangle$ will denote an averaging on T which will generally depends on the time.

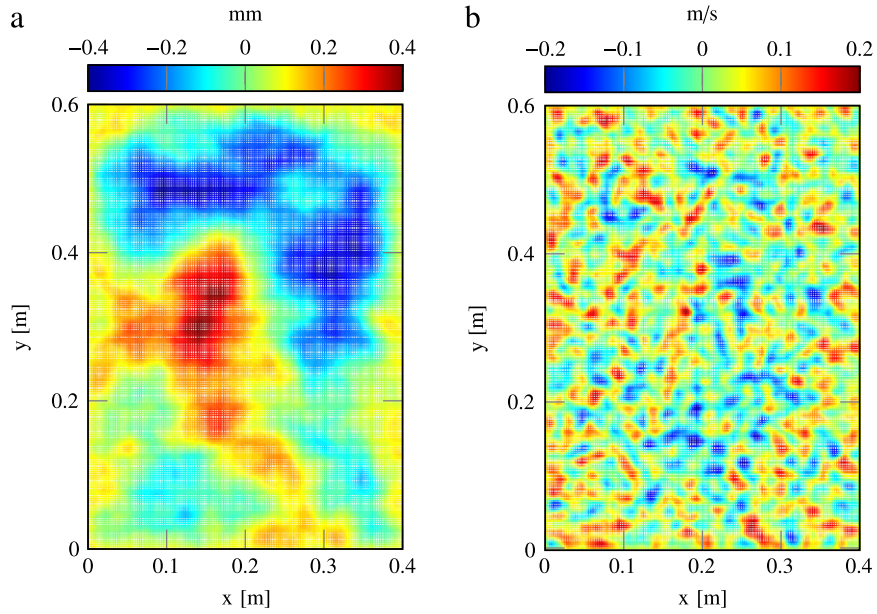

Fig. 1. (a) Displacement field in the turbulent regime for an undamped, perfectly flat plate of thickness $h = 0.1$ mm and dimensions $L_x \times L_y = 0.4 \times 0.6$ m^2. (b) Corresponding velocity field.

Table 1
Case studies.

	A_0 (N)	h (mm)	f_p (Hz)	S	Grid points
Case 1	10	1	75	0.4×0.6	102×153
Case 2	20	1	75	0.4×0.6	102×153
Case 3	30	1	75	0.4×0.6	102×153
Case 4	45	1	75	0.4×0.6	102×153
Case 5	70	1	75	0.4×0.6	102×153
Case 6	2.5	0.5	37.5	0.4×0.6	102×153
Case 7	5	0.5	37.5	0.4×0.6	102×153
Case 8	0.75	0.4	30	0.4×0.6	102×153
Case 9	1.5	0.4	30	0.4×0.6	102×153
Case 10	0.1	0.2	15	0.4×0.6	102×153
Case 11	0.02	0.1	7.5	0.4×0.6	144×216
Case 12	0.005	0.1	7.5	0.4×0.6	102×153
Case 13	1	0.5	20	1×2	114×227
Case 14	1.75	0.5	20	1×2	114×227
Case 15	2.5	0.5	20	1×2	114×227

The analysis for the injected power follows the same averaging rules. The injected power discrete time series is denoted by ε_n, from which the mean $\langle\varepsilon\rangle$ and the variance $\langle\varepsilon^2\rangle$ are calculated. The temporal average $\bar{\varepsilon}$ is defined as the mean over the total data.

A characteristic frequency f_c for the velocity power spectrum is here introduced as

$$f_c = \frac{\int \langle P_v(f)\rangle \, f \, df}{\int \langle P_v(f)\rangle \, df}, \tag{16}$$

with $P_v(f_c)$ also defining a characteristic spectral amplitude. Note that f_c should not be confused with the theoretical cut-off frequency $f_c^\star$ defined in Eq. (1). The characteristic frequency f_c will be used in the next section in order to quantify the self-similar dynamics of the spectra in the non-stationary cases.

4. Numerical results

This section presents the results obtained for the following cases:

(i) $R(\dot{w}, t) = 0$, $w_0(\mathbf{x}) = 0$ (perfectly flat, undamped plate);
(ii) $R(\dot{w}, t) = 0$, $w_0(\mathbf{x}) \neq 0$ (imperfect, undamped plate);
(iii) $R(\dot{w}, t) \neq 0$, $w_0(\mathbf{x}) = 0$ (perfectly flat, damped plate).

Simulations are also conducted by varying the dimensions S and the thickness h of the plate for different forcing amplitudes A_0 and frequencies f_p. The first part is devoted to periodically forced turbulence and the second to free turbulence (or decaying, when damping is added) after the forcing is stopped.

4.1. Periodically forced undamped turbulence

4.1.1. Perfect, undamped plates

Typical numerically obtained displacement and velocity fields are shown in Fig. 1 for illustration. The displacement field presents low frequency patterns; taking the velocity filters out these low frequencies resulting in a much more homogeneous field, meaning that velocity measurements at one point are relevant for the turbulent property of the whole plate as already mentioned in experiments having similar forcing schemes [17–19]. The anisotropy effects due to the local forcing have been evidenced and characterized experimentally by Miquel and Mordant [19].

A case study is first examined to serve as a master example of the type of analysis that has been conducted on all the simulations. It corresponds to case 1 in Table 1 considering a plate of thickness $h = 1$ mm, forced at $f_p = 75$ Hz with a forcing of amplitude $A_0 = 10$ N and a ramp time $t_0 = 0.5$ s (see Eq. (6), where t_1 is the whole duration of the simulation). The surface is $L_x \times L_y = 0.4 \times 0.6$ m^2 and the grid size is 102×153 points, corresponding to a sampling rate of 400 kHz for the time integration.

Fig. 2(a) shows the spectrogram (evolution of the frequency spectra with respect to time) of the velocity at the measurement point. It reveals the activated frequencies of the turbulent cascade as a function of time. The energy keeps flowing into the system, creating a never ending cascade where modes of higher frequency receive energy from the adjacent lower frequency modes. Fig. 2(b) shows the velocity power spectra at different stages of the dynamics. It is evident that for these simulations no stationary state exists: the spectra tend to occupy larger portions of the available frequency range as time goes by. It should be pointed out that the cascade front will develop up to half the sampling frequency of the computation (200 kHz in this case): when the cascade hits this limit, an artificial boundary reflects the energy back into the box, towards smaller frequencies. This is a peculiar,

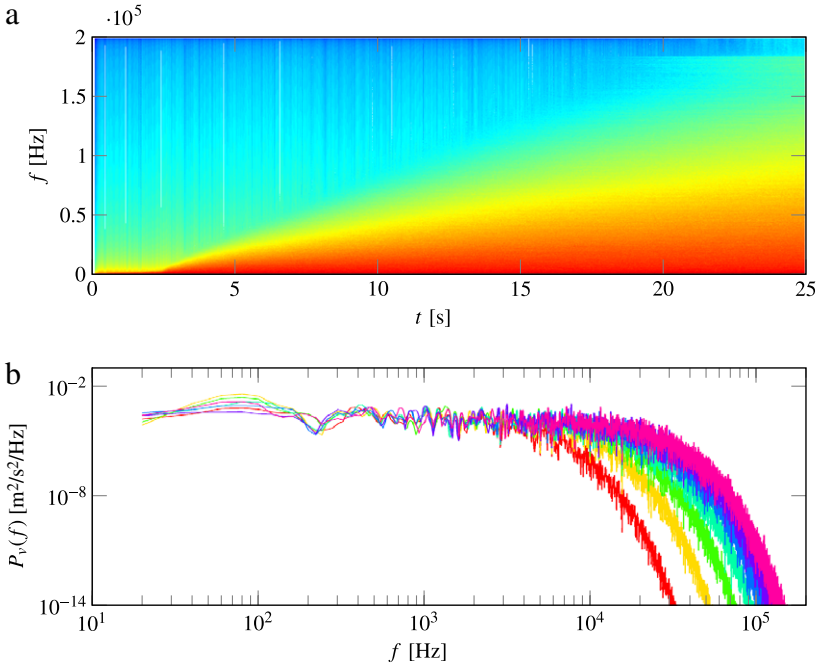

Fig. 2. (a) Spectrogram of the velocity for the perfect undamped plate of thickness $h = 1$ mm, forcing from 0 to 10 N in 0.5 s (case 1 from Table 1), and then kept constant. (b) Corresponding velocity power spectra computed every 2.5 s from 5 to 25 s.

unwanted numerical phenomenon that is not taken into account in the analysis. The simulation is stopped before the boundary reflection happens; in this way, the cascade can be regarded as developing within an infinite frequency domain. Fig. 3(a) shows that the evolution of the characteristic frequency $f_c(t)$ is linear, $f_c = c_f \cdot t$. The cascade front in Fig. 2 then develops to larger frequencies with a constant cascade velocity c_f. The spectral amplitude at the characteristic frequency $\langle P_v(f_c)\rangle$ in Fig. 3(b) is seen to be fairly constant over time. The power velocity spectra, rescaled using both the characteristic frequency f_c and amplitude $P_v(f_c)$, are displayed in Fig. 4. They all satisfactorily superimpose, indicating that the dynamics of the energy spectrum is self-similar. This allows us to write for the spectra

$$\langle P_v(f)\rangle = \langle P_v(f_c)\rangle\, \phi_P\left(\frac{f}{f_c}\right), \tag{17}$$

where their shapes are given by the unique function $\phi_P\,(f/f_c)$ (the subscript $_P$ stands for periodically forced turbulence).

The injected power during the self-similar dynamics is shown in Fig. 5(a): the fluctuations increase with time while the average stays constant. More precisely, Fig. 5(b) shows that $\langle \varepsilon^2\rangle = Dt$, and $\langle \varepsilon\rangle = \bar{\varepsilon}$. Hence, the self-similar dynamics originate with the injection of a stationary energy flux characterized by $\bar{\varepsilon}$. Meanwhile, the fluctuations of the injection flux grow following a diffusion-type behavior characterized by the coefficient D.

The analysis described above is now applied to 15 different cases, summarized in Table 1. For all cases, the self-similar dynamics display a constant injected power $\bar{\varepsilon}$, a linear growth of the variance of injected power $\langle \varepsilon^2\rangle$, a linear increase of f_c over time and constant $\langle P_v(f_c)\rangle$ has been observed. It is worth noting that the forcing values cover about four decades; this results in a large range for the mean injected power $\bar{\varepsilon}$. The thickness values cover one decade also. For each one of the cases, the cascade velocity c_f, the spectral amplitude at the characteristic frequency $\langle P_v(f_c)\rangle$, the diffusion coefficient D are calculated. These quantities are plotted in Fig. 6 as functions of combinations of $\bar{\varepsilon}$ and h having the same dimensions. It can be seen that for all cases a linear relationship is found, confirming the consistency of the dimensional argument. The constants of proportionalities are found from best linear fits:

$$\langle P_v(f_c)\rangle = 2.51 h(\bar{\varepsilon})^{1/3}, \tag{18a}$$

$$c_f = 0.20\frac{(\bar{\varepsilon})^{2/3}}{h^2}, \tag{18b}$$

$$D = 2.07\cdot 10^4 \frac{(\bar{\varepsilon})^{7/3}}{h}. \tag{18c}$$

In conclusion, the main result arising from the numerical simulations of the periodically forced undamped plate is a self-similar evolution of the power spectra. It is characterized by the progression towards higher frequencies of a steep cascade front, which leaves a steady self-similar spectrum in its wake. The self-similar progression is found to be linear with time and has been characterized by nondimensional numbers. The spectral amplitude at f_c is found to have a dependence on $(\bar{\varepsilon})^{1/3}$ (see Fig. 6) and the self-similar spectrum can be expressed as

$$P_v(f) = 0.42 h(\bar{\varepsilon})^{\frac{1}{3}} \Phi_P\left(\frac{f}{f_c}\right), \tag{19}$$

where $\bar{\varepsilon}$ is the mean injected power. In the absence of damping, the mean injected power can be confounded with the energy flux

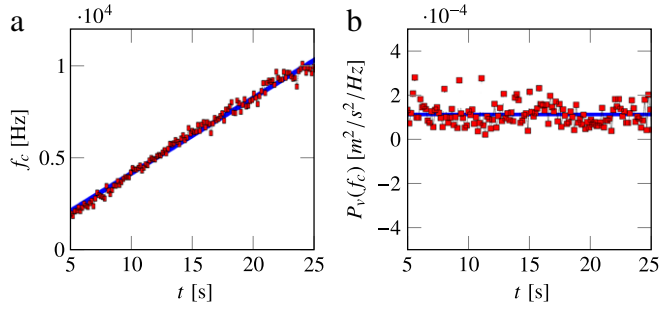

Fig. 3. (a) Time evolution of the characteristic frequency f_c, (b) corresponding spectral amplitude of the spectra shown in Fig. 2(b) (case 1 in Table 1). The characteristic frequency evolves as $f_c = c_f t$ with $c_f = 412.05$ s^{-2} and the mean amplitude is $\langle P_v(f_c)\rangle = 1.11\cdot 10^{-4}$ m^2/s^2/Hz.

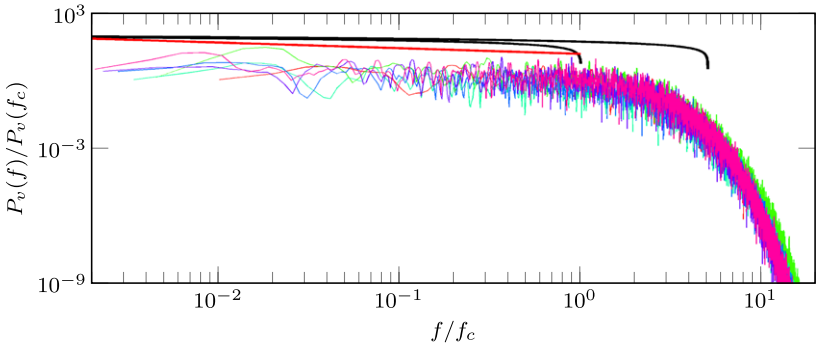

Fig. 4. Spectra of Fig. 2(b) but normalized using the characteristic frequency f_c and amplitude $P_v(f_c)$. Continuous red line shows a power law $f^{-\frac{1}{4}}$. Continuous black lines show the log correction $\log^{1/3}\left(\frac{f_c^\star}{f}\right)$ of the KZ spectrum, see Eq. (1), with $f_c^\star = f_c$ and $f_c^\star = 5f_c$. (For interpretation of the references to color in this figure legend, the reader is referred to the web version of this article.)

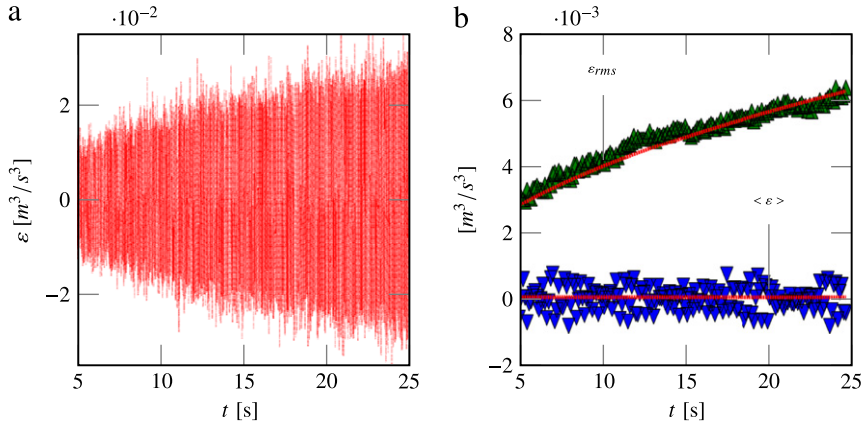

Fig. 5. Time evolution of the injected power for the perfect undamped plate (case 1 in Table 1). (a) Time series, (b) $\langle\varepsilon\rangle$ and $\varepsilon_{rms} = \sqrt{\langle\varepsilon^2\rangle}$. Continuous lines are best fits that give $\bar{\varepsilon} = 9.65 \cdot 10^{-5}$ m^3/s^3, and $D = 1.6 \cdot 10^{-6}$ m^6/s^7 (see the text).

transfer ε_c through scales. The progression of the cascade front towards higher frequencies is given by $f_c(t) = c_f t \propto \frac{\bar{\varepsilon}^{\frac{2}{3}}}{h^2} t$ (from Eq. (18b)). The function Φ_P displayed in Fig. 4 increases as frequencies decrease towards the forcing frequency f_p. A best-fit approximation of the slope of Φ_P indicates that it follows a power-law for low frequencies with a small exponent close to $-1/4$; see Fig. 4.

The self-similar solutions for the kinetic equation derived from the von Kármán plate equations are given in Appendix A. Considering a self-similar solution for the wave spectrum $n(k, t)$ of the form:

$$n(k, t) = t^{-q} f_1(kt^{-p}) = t^{-q} f_1(\xi), \tag{20}$$

one finds for the power frequency spectrum $P_v(\omega, t)$:

$$P_v(\omega, t) \sim f_1\left(\sqrt{\frac{\omega}{t}}\right) = g_1\left(\frac{\omega}{t}\right). \tag{21}$$

This relationship clearly evidenced that the frequency of the front must evolve linearly with time, which is retrieved by the numerical simulation. The function g_1 can be identified with the function Φ_P found numerically.

Let us now compare the self-similar spectrum with the KZ solution. As the theoretical cut-off frequency $f_c^\star$ cannot be related to a given physical quantity in our numerical framework, the KZ spectrum is built from Eq. (1) by selecting $f_c^\star = f_c$ and $f_c^\star = 5f_c$, and reported in Fig. 4. As one is interested in the power-law behavior in the low-frequency range, one can observe that selecting $f_c^\star = f_c$ or $f_c^\star = 5f_c$ has little influence on the slope comparison. It appears that even though the log-correction of the KZ spectrum cannot be discarded, the slope of the self-similar numerical solution appears to be a bit steeper.

Table 2
Case studies for the imperfect plate.

	A_0 (N)	h (mm)	f_p (Hz)	Z (mm)
Case 1	7	0.5	8.5	1
Case 2	3	0.5	8.5	1
Case 3	0.02	0.1	10.5	0.5
Case 4	0.01	0.1	10.5	0.5
Case 5	0.03	0.1	13	1
Case 6	0.02	0.1	8.5	0.1
Case 7	0.02	0.1	13	1
Case 8	0.01	0.1	8.5	0.1
Case 9	100	1	127	10
Case 10	70	1	127	10
Case 11	90	1	103	5
Case 12	60	1	103	5

The injected power fluctuation is found to increase as a diffusive law during the self-similar dynamics. A comprehensive interpretation of this behavior may be given by the model of injected power proposed in [43,44] for this system. In this work, the velocity $\dot{w}(\mathbf{x}_\mathcal{F}, t)$ at the forcing point is assumed to result from a turbulent feedback v described by the velocity spectrum, and a linear response of the deterministic forcing $\mathcal{F}(\mathbf{x}, t)$, say:

$$\dot{w}(\mathbf{x}_\mathcal{F}, t) = v + \mathcal{L}\mathcal{F}, \tag{22}$$

with $\mathcal{L}$ a linear operator. The feedback turbulent velocity is assumed to be statistically independent of the forcing. Thus, using Eq. (22) and the periodic forcing in Eq. (5) with $A(t) = A_0$, the mean

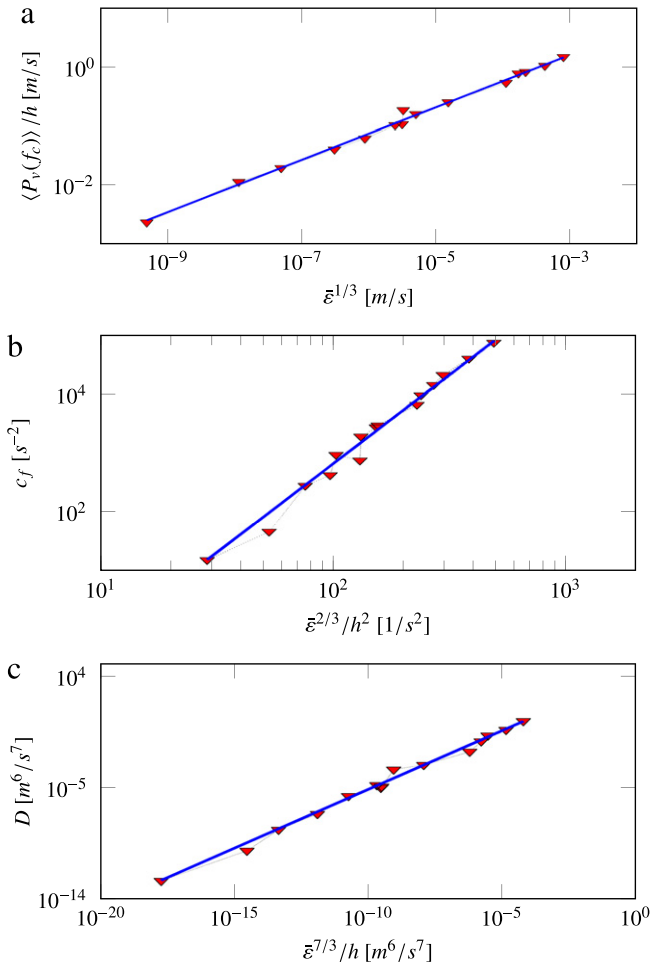

Fig. 6. Results of simulations for the perfect, undamped plate with a periodic forcing, for all the 15 cases reported in Table 1. (a) Spectral amplitude $\langle P_v(f_c)\rangle/h$, (b) cascade velocity c_f and (c) diffusion coefficient D.

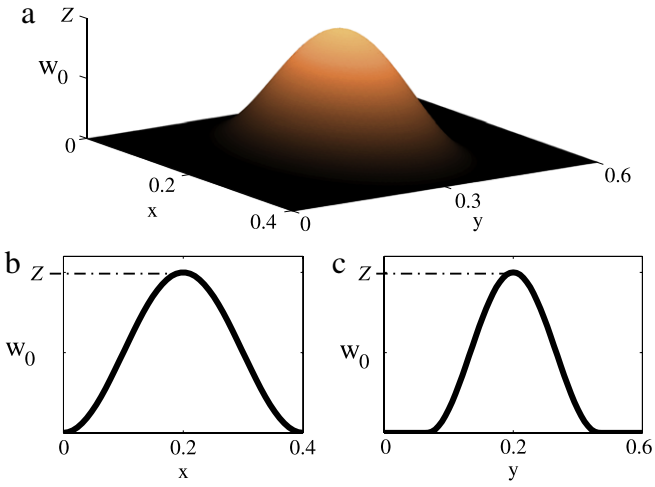

Fig. 7. Plate of dimensions $0.4 \times 0.6\ m^2$ with imperfection in the form of a raised cosine. (a) 3D view, (b) and (c) x and y axes views.

of the squared injected power becomes:

$$\langle(\mathcal{F}\dot{w})^2\rangle = \frac{A_0^2}{2}\langle v^2\rangle + \langle(\mathcal{L}\mathcal{F})^2\mathcal{F}^2\rangle. \tag{23}$$

After a sufficiently long time, the stationary forcing term will be negligible compared with the quadratic term that keeps increasing with time as the cascade propagates. Using Parseval's identity:

$$\langle v^2\rangle = \int_0^\infty P_v(f)df \tag{24}$$

and the expression of the self-similar time-dependent spectrum in Eq. (19), Eq. (23) becomes:

$$\langle(\mathcal{F}\dot{w})^2\rangle \sim \frac{A_0^2}{2}\langle v^2\rangle \propto A_0^2\frac{\bar{\varepsilon}t}{h}, \tag{25}$$

then

$$\langle\varepsilon^2\rangle \propto A_0^2\frac{\bar{\varepsilon}t}{h(\rho S)^2} \tag{26}$$

which gives the expected diffusive behavior. Hence, the injected power fluctuation is the consequence of a direct feedback of the propagation of the kinetic energy spectrum during the self-similar dynamics.

4.1.2. Imperfect, undamped plates

The effect of the presence of a plate imperfection on the turbulent dynamics is now investigated. Results are presented following the same procedure as for the perfect plate.

The static deformation $w_0(\mathbf{x})$ appearing in Eq. (2) is chosen in the form of a raised cosine

$$w_0(\mathbf{x}) = \frac{Z}{2}\left[1 + \cos\left(\frac{\pi\sqrt{(x-x_0)^2+(y-y_0)^2}}{L}\right)\right], \tag{27}$$

when $(x-x_0)^2 + (y-y_0)^2 \leq L^2$, and zero otherwise. Here Z is the static (vertical) deflection, L is the width and $\mathbf{x}_0$ is the center of the deformation. The plate area is $0.4 \times 0.6\ m^2$ and the width is here selected to be 0.2 m, and $\mathbf{x}_0$ is the center of the plate; see Fig. 7. Z is then a free parameter that changes case by case. This form of imperfection has been selected as it is close to what can be observed in experiments, where large plates are generally affected by a pattern of large wavelength. Our goal is thus to quantify the effect of a selected realistic geometric imperfection in order to assess its potential effect on the turbulence spectra. For the perfect plate with $w_0(\mathbf{x}) = 0$, the internal restoring force is symmetric so that only cubic nonlinearities are present in the von Kármán equations. However when an imperfection is considered, quadratic nonlinearity appears in the model equations and so three-wave processes are present in the dynamics.

A case study (case 11 in Table 2) is first examined. It corresponds to a plate with a thickness $h = 1$ mm, and a deformation $Z = 5$ mm as defined in Eq. (27). As the eigenfrequencies increase with the imperfection (see *e.g.* [29,27]), the excitation frequency is now shifted so as to remain in the vicinity of the fourth eigenfrequency, so that now $f_p = 103$ Hz, and the forcing amplitude is selected as $A_0 = 90$ N.

During the dynamics, it is observed that the velocity power spectra evolve almost identically to the case of the perfect plate, so that the spectrogram and power spectra of the imperfect plate are similar to those shown in Fig. 2. The characteristic frequency increases linearly with time while the characteristic amplitude remains fairly constant as shown in Fig. 8. The normalized spectra in Fig. 9 are superimposed according to a curve $\phi_P(f/f_c) = \langle P_v(f)\rangle/\langle P_v(f_c)\rangle$ indicating self-similar dynamics. The self-similar dynamics is also produced during a mean constant injection flux with diffusive-type fluctuations, as seen in Fig. 10.

A total of 12 simulations are considered for imperfect plates. The parameters are listed in Table 2. Note that the magnitude of the imperfection considered is large ($Z \geq h$), and of the order of what can be expected in real experiments. In particular, it has been shown in [45,27,46] that an imperfection of the order of the

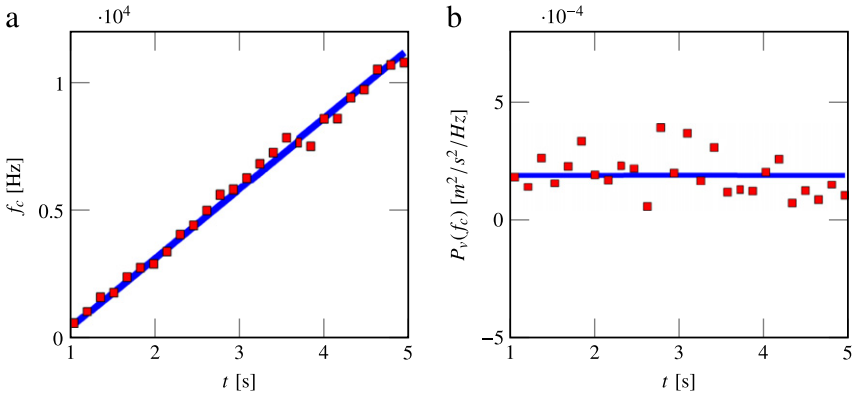

Fig. 8. Imperfect, undamped plate, case 11 of Table 2. (a) Time evolution of the characteristic frequency, (b) corresponding spectral amplitude. Continuous lines are best fit $f_c = c_f t$ with $c_f = 226\ \mathrm{s}^{-2}$ (a), and the mean amplitude $\langle P_v(f_c)\rangle = 2.66 \cdot 10^{-4}\ \mathrm{m}^2/\mathrm{s}^2/\mathrm{Hz}$.

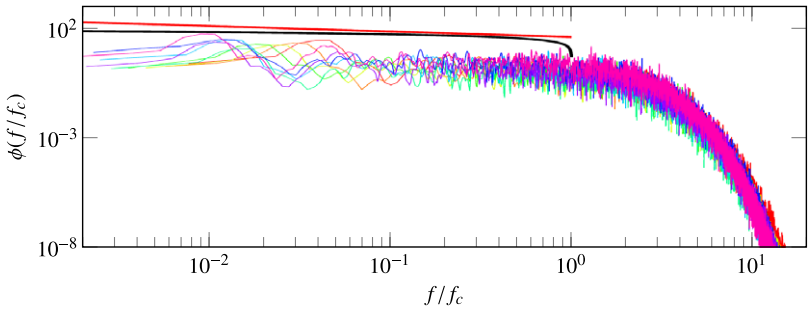

Fig. 9. Normalized velocity spectra using the characteristic frequency f_c and amplitude $P_v(f_c)$ (case 11 in Table 2). Continuous black line shows the log correction $\log^{1/3}\left(\frac{f_c^\star}{f}\right)$ of the KZ spectrum, see Eq. (1), with $f_c^\star = f_c$. Dashed red line shows a power law $f^{-\frac{1}{4}}$. (For interpretation of the references to color in this figure legend, the reader is referred to the web version of this article.)

thickness h is able to change the type of nonlinearity of the low frequency modes. For each one of the cases, the cascade velocity c_f, the spectral amplitude at the characteristic frequency $P_v(f_c)$ and the coefficient D are plotted as functions of combinations of $\bar{\varepsilon}$ and h. It can be seen that for all cases a linear relationship is found (Fig. 11):

$$\langle P_v(f_c)\rangle = 2.30 h \bar{\varepsilon}^{1/3} \tag{28a}$$

$$c_f = 0.19 \frac{\bar{\varepsilon}^{2/3}}{h^2} \tag{28b}$$

$$D = 1.86 \cdot 10^4 \frac{\bar{\varepsilon}^{7/3}}{h}. \tag{28c}$$

The scaling laws are identical to the perfect case, although the data are a bit more scattered in Fig. 11 than in Fig. 6. The obtained values for the proportional constants are also very close. The quadratic nonlinearity introduced by an imperfection is then hardly discernable in the turbulent cascade dynamics which indicates that the vibration amplitudes are sufficiently important so that the cubic term dominates the quadratic one; hence only the cubic nonlinearity seems to drive the main characteristics. In conclusion, the geometric imperfection retained in this study, and which has been selected as it provides insight into realistic imperfections one may encounter in experimental situations, has no effect on the main characteristics of the turbulent spectra. Hence it appears that plate imperfections should not be considered as a potential cause for explaining the discrepancies observed between theory derived for perfect plates and real experiments with unavoidable imperfections.

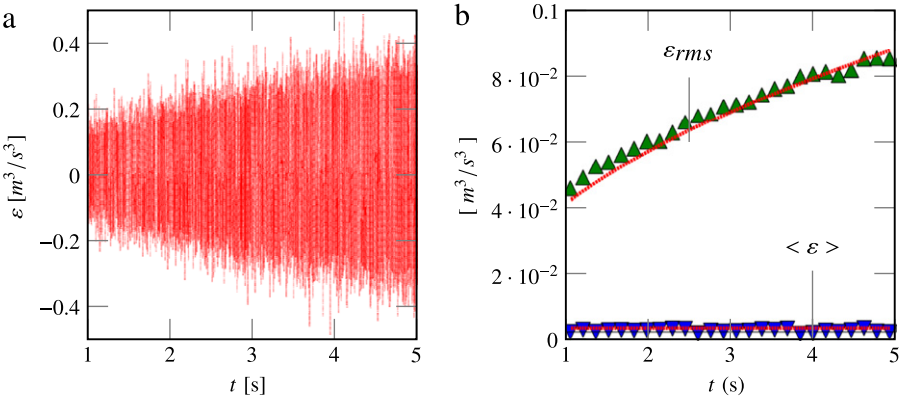

Fig. 10. Time evolution of the injected power for the imperfect undamped plate (case 11 in Table 2). (a) Time series, (b) $\langle\varepsilon\rangle$ and $\varepsilon_{rms} = \sqrt{\langle\varepsilon^2\rangle}$. Continuous lines are best fits: $\bar{\varepsilon} = 1.15 \cdot 10^{-5}\ \mathrm{m}^3/\mathrm{s}^3$, and $D = 0.0015\ \mathrm{m}^6/\mathrm{s}^7$ (see the text).

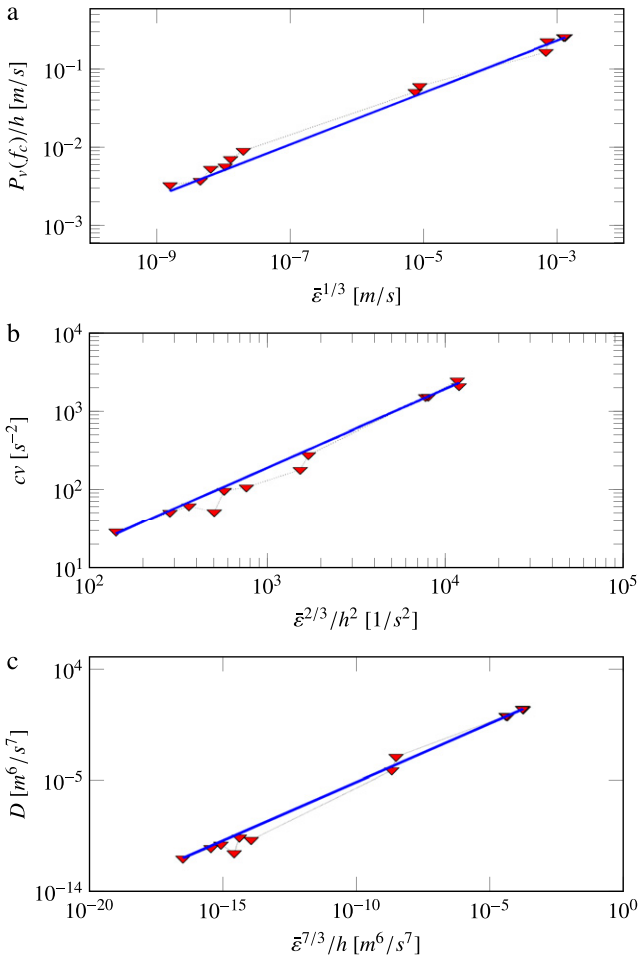

Fig. 11. Results of simulations for the imperfect, undamped plate with a periodic forcing, for the 12 cases reported in Table 2. (a) Spectral amplitude $\langle P_v(f_c)\rangle/h$, (b) cascade velocity c_f and (c) coefficient D.

In the remainder of the paper, the plate imperfections are no longer considered. The next section is devoted to the study of free (unforced) turbulence in order to highlight the effect of the pointwise forcing.

4.2. Free undamped turbulence

We now consider the case where the perfect, undamped plate, given an initial turbulent spectrum energy, is left free to vibrate in the absence of forcing and develops a cascade. The plate dimensions are $L_x \times L_y = 0.4 \times 0.6\ \mathrm{m}^2$, and the thickness is selected as $h = 0.1$ mm. The sampling rate is chosen as 40 kHz resulting in a grid size of 102×153 points. The excitation frequency is in the vicinity of the fourth eigenmode at 7.5 Hz. The forcing amplitude reaches $A_0 = 0.1$ N linearly after a duration $t_0 = 0.1$ s and is then abruptly stopped. The response of the system is shown over a long time duration in the spectrogram of Fig. 12(a). Even after stopping the external excitation, the number of excited modes keeps increasing slowly. Because of the slowness of this dynamics, the data analysis has been exceptionally changed with respect to the standard procedure explained in Section 3. Here the time window is $\tau = 0.1$ s and the number of spectra over which the average is taken is $M = 100$, resulting in a time $T = M\tau = 10$ s.

The velocity power spectra of the free decaying turbulence are shown at different stages of the dynamics in Fig. 12(b). The shape of the spectra changes abruptly just after the forcing is stopped. There is an evidence of a flattening in the low-frequency part of

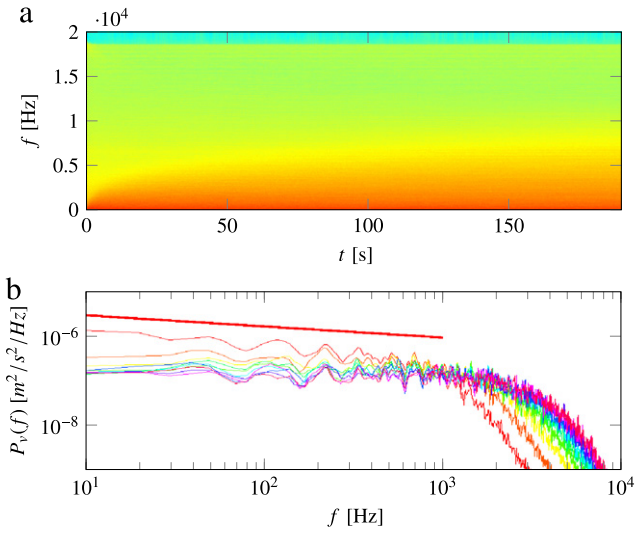

Fig. 12. (a) Spectrogram of the velocity of the perfect, undamped plate for which the forcing is stopped after 0.1 s. The plate is of thickness $h = 0.1$ mm and the sampling rate 40 kHz. (b) Corresponding velocity power spectra averaged over 10 s, displayed for time intervals of 30 s. The first one (red) is computed from 0.1s (i.e. the end of the forcing) to 10.1 s. Straight red line corresponds to the power law $f^{-1/4}$. (For interpretation of the references to color in this figure legend, the reader is referred to the web version of this article.)

the spectra, indicating once again the effect of the external forcing has on the power-law slope. On the other hand, the cascade front still progresses towards high frequencies even without forcing. The corresponding characteristic frequency evolution is shown in Fig. 13(a) and follows a clear 1/3 power law, significantly different from the linear dependence found for the case with external forcing. The energy conservation during the dynamics justifies the $-1/3$ power law best fit for the spectra amplitude in Fig. 13(b). More precisely, the characteristic frequency is found to behave as $f_c = at^{1/3}$ with $a = 331.5\ \mathrm{s}^{-\frac{4}{3}}$, whereas the spectral amplitude reads $P_v(f_c) = bt^{-1/3}$ with $b = 1.1 \cdot 10^{-7}\ \mathrm{m}^2\ \mathrm{s}^{-\frac{2}{3}}$. In order to express these dependences with nondimensional numbers, one can introduce the conserved quantities of the system, *i.e.* the total energy $\xi = \frac{h}{2}\int P_v(f)df$ of the turbulent fluctuations – once the forcing stopped the system is conservative – and the plate thickness h. The energy ξ may locally fluctuate since it is actually the energy of the whole plate that is conserved. However, for the point considered, it is found to keep reasonably constant at $\xi \approx 2 \cdot 10^{-8}\ \mathrm{m}^3/\mathrm{s}^2$ during the self-similar dynamics, as shown in Fig. 14. Using the relationships derived from the best fits obtained in Fig. 13 together with a dimensional analysis, one can reexpress the dependences as

$$f_c(t) = 0.45\frac{\xi^{\frac{2}{3}}}{h^2}t^{\frac{1}{3}} \qquad P_v(f_c) = 0.41h\xi^{\frac{1}{3}}t^{-\frac{1}{3}}. \tag{29}$$

The two constants now appearing in Eq. (29) should be universal, as are the nondimensional numbers derived from the analyses in previous sections.

The normalized spectra using both the characteristic frequency and corresponding spectra amplitude are shown in Fig. 15 for times larger than 10 s (i.e. after the low frequency spectra flattening). They all superimpose showing that the dynamics becomes self-similar with a spectrum universal shape Φ_F such that $P_v(f) = P_v(f_c)\Phi_F\left(\frac{f}{f_c}\right)$.

The progression of the cascade front towards higher frequencies must be accomplished by the presence of an energy flux ε_c. It can be estimated from the energy $d\xi_c$ of the activated modes between f_c and $f_c + df_c$ as the cascade propagates during the time interval

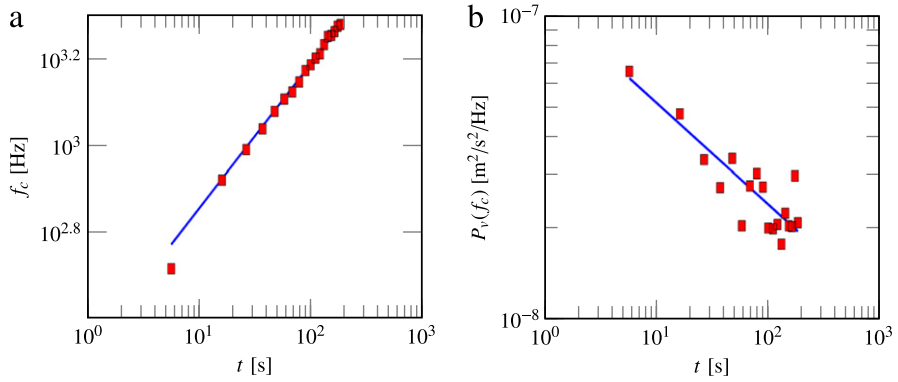

Fig. 13. Undamped free turbulence. (a) Time evolution of the characteristic frequency f_c and (b) corresponding spectral amplitude. Continuous lines are best fits $f_c = at^{1/3}$ with $a = 331.5\ \mathrm{s}^{-\frac{4}{3}}$ (a), and $P_v(f_c) = bt^{-1/3}$ with $b = 1.1 \cdot 10^{-7}\ \mathrm{m}^2\ \mathrm{s}^{-\frac{2}{3}}$ (b).

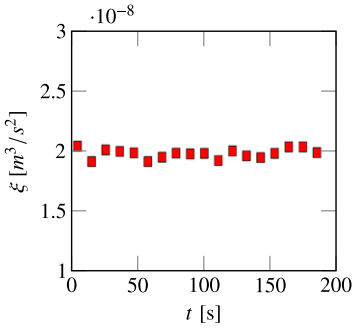

Fig. 14. Time evolution of the kinetic energy $\xi = \frac{h}{2}\int P_v(f)df$ for the free undamped turbulence.

dt, $\varepsilon_c = \frac{d\xi_c}{dt} = \frac{h}{2}P_v(f_c)\frac{df_c}{dt}$. Using both evolutions in Eq. (29), the estimation gives:

$$\varepsilon_c = 0.03\xi t^{-1}. \tag{30}$$

The spectrum in the self-similar dynamics of free turbulence can thus be expressed as:

$$P_v(f) = 13.34h\varepsilon_c^{\frac{1}{3}}\Phi_F\left(\frac{f}{f_c}\right). \tag{31}$$

As for the first case with periodic forcing, the dependence of the frequency front in $t^{1/3}$ can be derived from the theoretical kinetic equation governing the dynamics of the wave spectrum for vibrating plates. Following the calculations presented in Appendix A, and considering now that, for the self-similar solution of the form given by Eq. (20), the total energy of the system is conserved, one finds that the power frequency spectrum should fulfill the relationship:

$$P_v(\omega, t) \sim t^{-1/3}f_2\left(\sqrt{\frac{\omega}{t^{1/3}}}\right) = t^{-1/3}g_2\left(\frac{\omega}{t^{1/3}}\right). \tag{32}$$

This theoretical results clearly exhibits the fact that the frequency front should evolve as $t^{1/3}$ while the total energy as $t^{-1/3}$. In this case of free turbulence, the function g_2 can now be directly identified from the numerical solution Φ_F.

Let us now compare the self-similar solution with the theoretical KZ spectrum for vibrating plates. Because of the spectral flattening highlighted in Fig. 12(b), one can observe that the function Φ_F is now very close to the log-correction of the theoretical KZ spectrum for vibrating plates, as displayed in Fig. 15, and shown here for $f_c^\star = f_c$. The similarity between the self-similar spectrum of decaying turbulence with the stationary KZ spectrum has already been mentioned for surface gravity waves [34] and capillary waves [35,37,36]. The comparison between the self-similar spectra of periodically forced turbulence (Fig. 4) and free turbulence (Fig. 15) shows a steeper slope when forcing is present. This result should be retrieved in a more realistic case where damping is also considered and should corroborate the experimental results shown in [20]. The aim of the last section is thus to verify this numerically in the case of a decaying turbulence.

4.3. Damped turbulence

The effect of the forcing is now studied in a damped case. The plate dimensions are $L_x \times L_y = 0.4 \times 0.6\ \mathrm{m}^2$, the grid size is 102×153 and $h = 1$ mm. The damping introduced in Eq. (4) is selected as $\sigma_0 = 0.5\ \mathrm{s}^{-1}$. The forcing frequency is $f_p = 75$ Hz, with a forcing amplitude of $A_0 = 140$ N and a ramp time $t_0 = 0.5$ s. The forcing remains periodic from 0.5 to 3.5 s ($t_1 = 4$ s in Eq. (6)) and then abruptly stopped at $t = 4$ s.

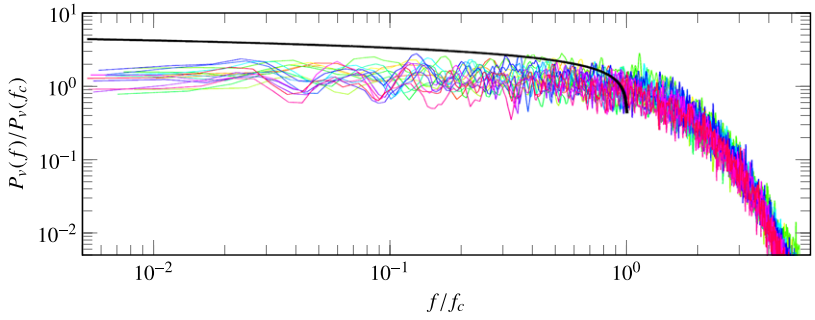

Fig. 15. Free undamped turbulence. Normalized velocity power spectra of Fig. 12(b) for $t > 10$ s during the self-similar dynamics. Black line shows the log correction $\log^{1/3}\left(\frac{f_c^\star}{f}\right)$ of the KZ spectrum, Eq. (1), with $f_c^\star = f_c$.

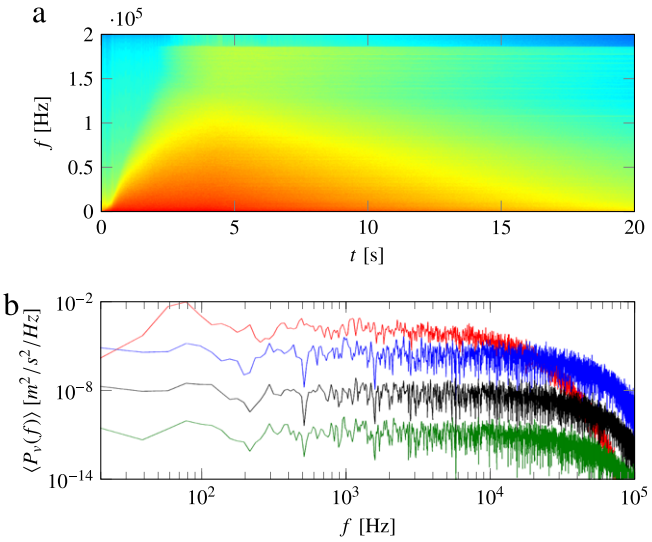

Fig. 16. (a) Spectrogram of the velocity for the perfect damped plate. (b) Corresponding velocity power spectra averaged over $T = 0.15$ s computed every 5 s from 5 to 20 s.

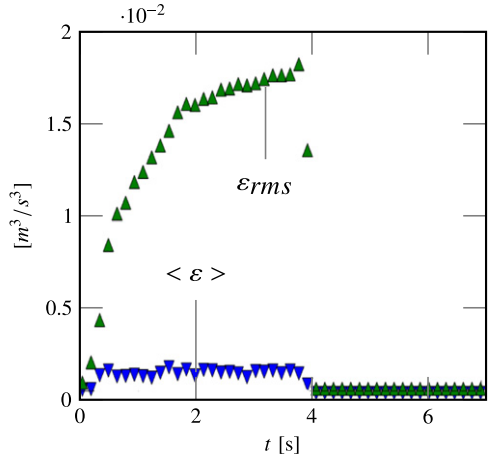

Fig. 17. Time evolution of the injected power, $\langle \varepsilon \rangle$ and $\varepsilon_{rms} = \sqrt{\langle \varepsilon^2 \rangle}$ for the decaying turbulence experiment shown in Fig. 16.

The response of the damped system is shown over 20 s of duration in the spectrogram in Fig. 16(a). The spectra reach a nearly steady state just before $t = 4$ s that corresponds to the time at which the forcing is stopped. Meanwhile, the injected power remains fairly constant in Fig. 17, $\langle \varepsilon \rangle (t) \simeq \bar{\varepsilon}$, and the characteristic frequency grows, just as for the undamped case studied in Section 4.1. The main difference is that the characteristic frequency (Fig. 18) will saturate to a constant value once the statistical steady state of turbulent energy will be reached. In other words, the cascade velocity front decreases towards zero when approaching the steady state.

As the cascade progresses to higher frequencies, more and more modes are activated, which results in an increase of the dissipation flux ε_d since each mode has a linear energy loss parameterized by σ_0 that should be compensated by the incoming flux. Hence, less and less energy flux ε_c is available to propagate the cascade front velocity, since $\langle \varepsilon_c \rangle (t) = \bar{\varepsilon} - \langle \varepsilon_d \rangle (t)$. Once the forcing is stopped at $t = 4$ s, the characteristic frequency overshoots as shown in Fig. 18 and then sharply saturates. The drastic increase of the characteristic frequency is provoked by the flattening of the spectral shape at low frequencies as observed in Fig. 16(b).

The effect of the pointwise forcing evidenced in previous sections is here retrieved for the damped dynamics. The numerical experiment shown here shares similarities with the experimental result of [20], where the spectral flattening was also observed in the decaying turbulence regime. Once the forcing stopped, the spectrum simply decreases exponentially as $e^{-2\sigma_0 t}$ as expected by a pure damping linear dynamics; see Fig. 18(b). Actually one can observe that the nonlinear dynamics are still present but very weak since the nonlinear propagation depends on the vanishing turbulent energy $\xi(t)$. Note that selecting other damping laws should lead to different behaviors in the decaying regime, resulting from the competition between the nonlinear propagation effect with the energy losses, both of which having different frequency-dependences associated to different timescales. Here the damping law is frequency independent so that the results lend themselves to an easy physical interpretation.

5. Discussion and concluding remarks

The nonlinear dynamics of turbulent vibrating plates has been studied numerically with a finite-difference, energy-conserving scheme including a pointwise forcing together with realistic boundary conditions. The most important results have been obtained in the absence of damping, in the framework of non-stationary wave turbulence. Self-similar solutions for the energy spectrum have been exhibited for a wide range of parameter variations. The simulations display the presence of a front propagating to high frequencies. With pointwise forcing, this propagation is linear with time, whereas for free turbulence the dependence is in $t^{1/3}$. These self-similar behaviors can be directly retrieved from the kinetic equation by analyzing the admissible self-similar solutions. From the numerical solutions, one is thus able to get a numerical value for the self-similar functions in non-stationary wave turbulence for plates, for the two cases studied in this paper, with and without external forcing. Comparing the shape of these numerically obtained functions, one observes that they share similarities with the theoretical KZ spectrum computed by [14], albeit exhibiting interesting differences. In the case of a pointwise forcing, a steeper slope is observed as compared to the free undamped turbulence. Note also that the power 1/3 dependence on the energy flux is numerically retrieved.

This observation is robust to adding the damping in the simulations and thus recovers experimental results shown in [20]. It can thus be concluded that the local pointwise forcing has a measurable effect on the slope in the low-frequency range. This effect has been related in [20] to an anisotropy induced by the presence of the shaker. A direct extension of the results presented herein should thus to compute spatial spectra in order to verify numerically that the same argument holds.

For the first time, our numerical set-up allows for an investigation of the effect of a geometrical imperfection on the turbulent dynamics. The results, obtained in a non-stationary framework, clearly indicates that perfect and imperfect plates present identical characteristics in the WT regime. This emphasizes the fact that in this regime the cubic nonlinear terms dominate the quadratic ones, which thus have no measurable effect on the spectral characteristics of the WT. Note however that this is not true for the regimes of transition to turbulence that involve weaker excitation amplitudes [28,29]. Note also that only a simple, low-frequency pattern has been introduced as a geometric imperfection, in order to present numerical results close to what can be expected in real-life situations. The conclusions, based on numerical experiments, are only valid for those cases. Extensions of the present work could consider more complex geometric imperfections, with smaller wavelengths, in order to continue the quantification of the transition between perfect and imperfect plates' turbulent dynamics.

Finally, dimensional arguments have been used in order to properly quantify the results in non-stationary cases. As no

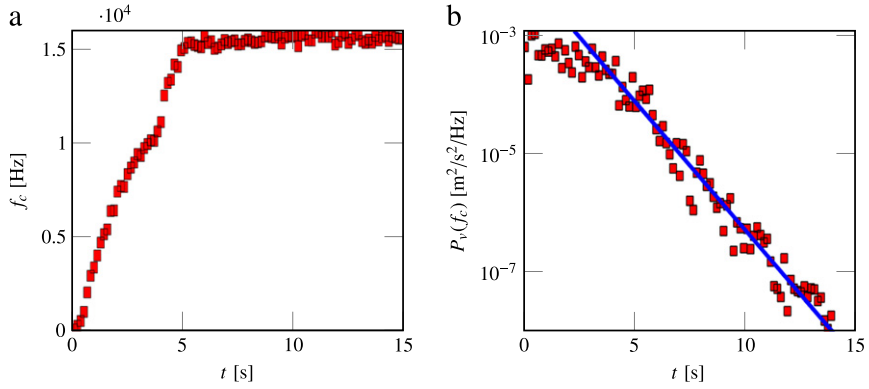

Fig. 18. (a) Time evolution of the characteristic frequency f_c and (b) corresponding spectral amplitude decreasing as $\langle P_v(f_c)\rangle = 0.012e^{-2\sigma_0 t}$ of the spectra shown in Fig. 16, with $\sigma_0 = 0.5\ \mathrm{s}^{-1}$ (blue thick line).

theoretical prediction for the non-stationary evolution of systems with log-corrected spectra exist at the present time, we believe the results shown here could be used so as to ascertain a theoretical development that may predict the observations reported in this contribution.

Acknowledgments

S. Bilbao was supported by the European Research Council, under Grant number StG-2011-279068-NESS. The authors want to thank Christophe Josserand for a fruitful discussion on the collision integral.

Appendix. Self-similar solutions for non-stationary wave turbulence in plates

This appendix is devoted to the derivation of self-similar solutions from the kinetic equation describing the wave turbulence in the von Kármán plate equations. Following the theoretical calculations reported by Düring et al. [14], the 4-waves kinetic equation has the general expression given by Zakharov et al. [2], and reads

$$\frac{\partial n(\mathbf{k},t)}{\partial t} = I(\mathbf{k}), \tag{A.1}$$

with $n(\mathbf{k},t) \equiv n_{\mathbf{k}}$ the wave spectrum and $I(\mathbf{k})$ the collision integral, the expression of which can be found in [14]:

$$I(\mathbf{k}) = 12\pi \int |J_{k123}|^2 f_{k123}\delta(\mathbf{k}+s_1\mathbf{k}_1+s_2\mathbf{k}_2+s_3\mathbf{k}_3) \times \delta(\omega_k+s_1\omega_1+s_2\omega_2+s_3\omega_3)d\mathbf{k}_1 d\mathbf{k}_2 d\mathbf{k}_3, \tag{A.2}$$

where J_{k123} stands for the interaction term and f_{k123} is such that

$$f_{k123} = \sum_{s_1,s_2,s_3} n_{\mathbf{k}} n_{\mathbf{k}_1} n_{\mathbf{k}_2} n_{\mathbf{k}_3} \left(\frac{1}{n_{\mathbf{k}}} + \frac{s_1}{n_{\mathbf{k}_1}} + \frac{s_2}{n_{\mathbf{k}_2}} + \frac{s_3}{n_{\mathbf{k}_3}}\right). \tag{A.3}$$

Following [2], let us introduce a self-similar solution for the non-stationary evolution, depending only on the wavevector modulus, as

$$n(\mathbf{k},t) = t^{-q} f(kt^{-p}) = t^{-q} f(\eta). \tag{A.4}$$

Plugging this ansatz in the kinetic equation (A.1), and taking into account the expression of $|J_{k123}|^2$ found in [14], one gets

$$-t^{-q-1}\left[qf(\eta) + p\eta f'(\eta)\right] = I(\eta)t^{-3q+2p}, \tag{A.5}$$

so that a solution of the form (A.4) is possible only if the condition $-q-1 = -3q+2p$ is satisfied. It can be rewritten as

$$2(q-p) = 1. \tag{A.6}$$

Let us introduce the total energy of the distribution

$$\xi = \int \omega\, n_{\mathbf{k}}\, d\mathbf{k} \tag{A.7}$$

and consider the two cases numerically studied:

Case 1: The plate is forced by a sinusoidal pointwise forcing of constant amplitude and excitation frequency. In this case the total energy increases linearly with time so that $\xi \sim t$.

Case 2: The plate is left free to vibrate, given an amount of energy as the initial condition. In this case the total energy is constant so that $\xi \sim t^0$.

Substituting (A.4) into (A.7) one obtains a second relationship between p and q, which reads, depending on the case considered

$$4p - q = \begin{cases} 1 & \text{for case 1} \\ 0 & \text{for case 2.} \end{cases} \tag{A.8}$$

Solving for (p,q) in both cases give

$$\text{case 1}: \ p = 1/2, \qquad q = 1, \tag{A.9}$$

$$\text{case 2}: \ p = 1/6, \qquad q = 2/3. \tag{A.10}$$

The last step consists in expressing the self-similar solution for $P_v(\omega)$ the power spectrum of the transverse velocity $v = \dot{w}$ used in the analysis, which is related to the power spectrum of the displacement $P_w(\omega)$ by a proportionality relationship $P_v(\omega) \propto \omega^2 P_w(\omega)$. Using the space–frequency relationship $P_w(\omega)d\omega \propto P_w(k)kdk$, together with the dispersion relation, one finds $P_w(\omega) \propto P_w(k)$, such that $P_v(\omega) \propto k^4 P_w(k)$. Finally, using the relationship $P_w(k) \propto \frac{n_k}{\omega}$ given in [14], one obtains finally $P_v(\omega,t) \propto k^2 n(k,t)$, so that the self-similar solutions for $P_v(\omega,t)$ finally reads for the general case with $n_{\mathbf{k}}$ given by Eq. (A.4):

$$P_v(\omega,t) \sim t^{2p-q} f(\omega^{1/2} t^{-p}). \tag{A.11}$$

Specifying now the solutions for (p,q) found for the two cases under study, one obtains for case 1:

$$P_v(\omega,t) \sim f_1\left(\sqrt{\frac{\omega}{t}}\right) = g_1\left(\frac{\omega}{t}\right), \tag{A.12}$$

and for case 2:

$$P_v(\omega,t) \sim t^{-1/3} f_2\left(\sqrt{\frac{\omega}{t^{1/3}}}\right) = t^{-1/3} g_2\left(\frac{\omega}{t^{1/3}}\right), \tag{A.13}$$

where $g_{1,2}$ (or $f_{1,2}$) have been indexed with respect to case 1 and case 2, and are functions to be defined.

References

[1] S. Nazarenko, Wave Turbulence, Springer-Verlag, Berlin, Heidelberg, 2011.
[2] V. Zakharov, V. L'vov, G. Falkovich, Kolmogorov Spectra of Turbulence 1: Wave Turbulence, in: Series in Nonlinear Dynamics, Springer, 1992.
[3] A. Newell, S. Nazarenko, L. Biven, Wave turbulence and intermittency, Physica D 152–153 (2001).
[4] U. Frisch, Turbulence, Cambridge University Press, Cambridge, 1995.
[5] V.E. Zakharov, N.N. Filonenko, Energy spectrum for stochastic oscillations of surface of a liquid, J. Appl. Mech. Tech. Phys. 8 (1967) 37.
[6] A.N. Pushkarev, V.E. Zakharov, Turbulence of capillary waves, Phys. Rev. Lett. 76 (1996) 3320–3323.
[7] V.E. Zakharov, N.N. Filonenko, Energy spectrum for stochastic oscillations of surface of a liquid, Sov. Phys. Dokl. 11 (1967) 881–883.
[8] M. Onorato, A.R. Osborne, M. Serio, D. Resio, A. Pushkarev, V.E. Zakharov, C. Brandini, Freely decaying weak turbulence for sea surface gravity waves, Phys. Rev. Lett. 89 (2002) 144501.
[9] E. Falcon, C. Laroche, S. Fauve, Observation of gravity—capillary wave turbulence, Phys. Rev. Lett. 98 (2007) 094503.
[10] S. Galtier, S. Nazarenko, A. Newell, A. Pouquet, A weak turbulence theory for incompressible magnetohydrodynamics, J. Plasma Phys. 63 (2000) 447–488.
[11] S. Galtier, S. Nazarenko, A. Newell, A. Pouquet, Anisotropic turbulence of shear-Alfvèn waves, Astrophys. J. Lett. 564 (2002) L49–L52.
[12] W. Vinen, Classical character of turbulence in a quantum liquid, Phys. Rev. B 61 (2000) 1410–1420.
[13] W. Vinen, Decay of superfluid turbulence at a very low temperature: the radiation of sound from a Kelvin wave on a quantized vortex, Phys. Rev. B 64 (2001) 134520.
[14] G. Düring, C. Josserand, S. Rica, Weak turbulence for a vibrating plate: can one hear a Kolmogorov spectrum? Phys. Rev. Lett. 97 (2006) 025503.
[15] T. von Kármán, Festigkeitsprobleme im Maschinenbau, Encyklopadie Math. Wiss. 4 (1910) 311–385.
[16] O. Thomas, S. Bilbao, Geometrically nonlinear flexural vibrations of plates: in-plane boundary conditions and some symmetry properties, J. Sound Vib. 315 (2008) 569–590.
[17] A. Boudaoud, O. Cadot, B. Odille, C. Touzé, Observation of wave turbulence in vibrating plates, Phys. Rev. Lett. 100 (2008) 234504.
[18] N. Mordant, Are there waves in elastic wave turbulence? Phys. Rev. Lett. 100 (2008) 234505.
[19] B. Miquel, N. Mordant, Nonlinear dynamics of flexural wave turbulence, Phys. Rev. E 84 (2011) 066607.
[20] B. Miquel, N. Mordant, Nonstationary wave turbulence in an elastic plate, Phys. Rev. Lett. 107 (2011) 034501.
[21] T. Humbert, O. Cadot, G. Düring, C. Josserand, S. Rica, C. Touzé, Wave turbulence in vibrating plates: the effect of damping, Europhys. Lett. 102 (2013) 30002.
[22] N. Yokoyama, M. Takaoka, Weak and strong wave turbulence spectra for elastic thin plate, Phys. Rev. Lett. 110 (2013) 105501.
[23] B. Miquel, A. Alexakis, N. Mordant, Role of dissipation in flexural wave turbulence: from experimental spectrum to Kolmogorov–Zakharov spectrum, Phys. Rev. E (2014) submitted for publication.
[24] B. Miquel, Études expérimentales et numériques de la turbulence d'ondes de flexion (Ph.D. thesis), Université Pierre et Marie curie, Paris, 2013.
[25] B. Miquel, A. Alexakis, C. Josserand, N. Mordant, Transition from wave turbulence to dynamical crumpling in vibrated elastic plates, Phys. Rev. Lett. 111 (2013) 054302.
[26] Z. Celep, Free flexural vibration of initially imperfect thin plates with large elastic amplitudes, ZAMM Z. Angew. Math. Mech. 56 (1976) 423–428.
[27] C. Camier, C. Touzé, O. Thomas, Non-linear vibrations of imperfect free-edge circular plates and shells, Eur. J. Mech. A Solids 28 (2009) 500–515.
[28] C. Touzé, O. Thomas, M. Amabili, Transition to chaotic vibrations for harmonically forced perfect and imperfect circular plates, Internat. J. Non-Linear Mech. 46 (2011) 234–246.
[29] C. Touzé, S. Bilbao, O. Cadot, Transition scenario to turbulence in thin vibrating plates, J. Sound Vib. 331 (2012) 412–433.
[30] S. Bilbao, A family of conservative finite difference schemes for the dynamical von Kármán plate equations, Numer. Methods Partial Differential Equations 24 (2008) 193–216.
[31] E. Hairer, C. Lubich, G. Wanner, Geometric Numerical Integration, Structure-Preserving Schemes for Ordinary Differential Equations, Springer, 2006.
[32] G. Falkovich, A. Shafarenko, Nonstationary wave turbulence, J. Nonlinear Sci. 1 (1991) 457–480.
[33] C. Connaughton, A. Newell, Y. Pomeau, Non-stationary spectra of local wave turbulence, Physica D 184 (2003) 64–85.
[34] R. Bedard, S. Lukaschuk, S. Nazarenko, Non-stationary regimes of surface gravity wave turbulence, JETP Lett. 97 (2013) 459–465.
[35] G.V. Kolmakov, A.A. Levchenko, M.Y. Brazhnikov, L.P. Mezhov-Deglin, A.N. Silchenko, P.V.E. McClintock, Quasiadiabatic decay of capillary turbulence on the charged surface of liquid hydrogen, Phys. Rev. Lett. 93 (2004) 074501.
[36] L. Deike, M. Berhanu, E. Falcon, Decay of capillary wave turbulence, Phys. Rev. E 85 (2012) 066311.
[37] G. Kolmakov, Decay of capillary turbulence on the surface of a viscous liquid, JETP Lett. 83 (2006) 58–63.
[38] G.L. Ostiguy, S. Sassi, Effects of initial geometric imperfections on dynamic behaviour of rectangular plates, Nonlinear Dynam. 3 (1992) 165–181.
[39] L.D. Landau, L.P. Pitaevskii, E.M. Lifshitz, A.M. Kosevich, Theory of Elasticity, third ed., Butterworth–Heinemann, 1986.
[40] M. Ducceschi, C. Touzé, S. Bilbao, C. Webb, Nonlinear dynamics of rectangular plates: investigation of modal interaction in free and forced vibrations, Acta Mech. 225 (2014) 213–232.
[41] A. Chaigne, C. Lambourg, Time-domain simulation of damped impacted plates. I: theory and experiments, J. Acoust. Soc. Am. 109 (2001) 1422–1432.
[42] S. Bilbao, Numerical Sound Synthesis: Finite Difference Schemes and Simulation in Musical Acoustics, Wiley, 2009.
[43] O. Cadot, A. Boudaoud, C. Touzé, Statistics of power injection in a plate set into chaotic vibration, Eur. Phys. J. B 66 (2008) 399–407.
[44] O. Cadot, C. Touzé, A. Boudaoud, Linear versus nonlinear response of a forced wave turbulence system, Phys. Rev. E 82 (2010) 046211.
[45] C. Touzé, O. Thomas, Non-linear behaviour of free-edge shallow spherical shells: effect of the geometry, Internat. J. Non-Linear Mech. 41 (2006) 678–692.
[46] C. Touzé, C. Camier, G. Favraud, O. Thomas, Effect of imperfections and damping on the type of non-linearity of circular plates and shallow spherical shells, Math. Probl. Eng. 2008 (2008) Article ID 678307.